International Journal of Minerals, Metallurgy and Materials
Volume 28, Number 10, October 2021, Page 1666
https://doi.org/10.1007/s12613-021-2286-2

Ultrafine nano-scale Cu_2Sb alloy confined in three-dimensional porous carbon as an anode for sodium-ion and potassium-ion batteries

Dan Wang[1,2,3], *Qun Ma*[1)], *Kang-hui Tian*[1)], *Chan-Qin Duan*[1)], *Zhi-yuan Wang*[1,2,3)], *and Yan-guo Liu*[1,2,3)]

1) School of Materials Science and Engineering, Northeastern University, Shenyang 110819, China
2) School of Resources and Materials, Northeastern University at Qinhuangdao, Qinhuangdao 066004, China
3) Key Laboratory of Dielectric and Electrolyte Functional Material Hebei Province, Qinhuangdao 066004, China
(Received: 31 December 2020; revised: 25 March 2021; accepted: 26 March 2021)

Abstract: Ultrafine nano-scale Cu_2Sb alloy confined in a three-dimensional porous carbon was synthesized using NaCl template-assisted vacuum freeze-drying followed by high-temperature sintering and was evaluated as an anode for sodium-ion batteries (SIBs) and potassium-ion batteries (PIBs). The alloy exerts excellent cycling durability (the capacity can be maintained at 328.3 $mA{\cdot}h{\cdot}g^{-1}$ after 100 cycles for SIBs and 260 $mA{\cdot}h{\cdot}g^{-1}$ for PIBs) and rate capability (199 $mA{\cdot}h{\cdot}g^{-1}$ at 5 $A{\cdot}g^{-1}$ for SIBs and 148 $mA{\cdot}h{\cdot}g^{-1}$ at 5 $A{\cdot}g^{-1}$ for PIBs) because of the smooth electron transport path, fast Na/K ion diffusion rate, and restricted volume changes from the synergistic effect of three-dimensional porous carbon networks and the ultrafine bimetallic nanoalloy. This study provides an ingenious design route and a simple preparation method toward exploring a high-property electrode for K-ion and Na-ion batteries, and it also introduces broad application prospects for other electrochemical applications.

Keywords: copper–antimony alloy; anode; porous carbon; potassium-ion batteries; sodium-ion batteries

1. Introduction

Nowadays, considering the rare reserve and high price of lithium, as well as the ever-increasing demand for large-scale energy storage and electric automobiles, potassium-ion batteries (PIBs) and sodium-ion batteries (SIBs) with abundant resources and low cost are promising supplements or substitutes to lithium-ion batteries because K and Na belong to the same IA main group and display similar properties to Li. However, the larger ion radius of K^+/Na^+ (Na^+: 0.102 nm; K^+: 0.138 nm) compared with Li^+ (Li^+: 0.076 nm) usually limits their diffusion and insertion into electrode materials and leads to sluggish reaction dynamics and poor cycling stability [1–3]. Therefore, it's a great challenge and urgent demand to design suitable electrode materials for PIBs and NIBs.

Alloy-based anode materials, especially antimony, have a high theoretical specific capacity (660 $mA{\cdot}h{\cdot}g^{-1}$) and a suitable working potential for application in alkali ion batteries; however, they are subject to volume expansion (up to 400%) during the charging/discharging procedure, which usually creates electrode pulverization and leads to deteriorated cycling performance and rate capability [4–7]. To address the above issues, three effective strategies are generally adopted: introduce inactive/active ingredients (Sn, Bi, Co, etc) [8–10] to Sb to stabilize the electrode structure; fabricate nano-sized materials (nanowire, nanofiber, nanotube) [11–13] to relieve the internal stress; combine Sb with a buffer substance, such as carbon materials (graphene, hard carbon, soft carbon) [14–16] to mitigate the volume expansion of Sb and increase the electrode conductivity. Although many Sb-based nanocomposites have been reported, problems such as the aggregation of nanoparticles and low cohesive force between the alloy and the carbon still exist. Therefore, new Sb-based composite materials with a more stable structure and a more convenient and rational synthesized method are required. Three-dimensional (3D) porous carbon has been used as a highly efficient buffer to relieve the volume expansion of alloy, which can effectively suppress nanoparticle aggregation. Moreover, employing an *in-situ* method to fabricate the alloy/3D porous carbon composite can effectively solve the weak binding force between the alloy and the carbon. In our previous work, we successfully fabricated a series of Sb-base alloy/3D porous carbon composites, including FeSb/C, SnSb/C, and BiSb/C, all of which displayed different electrochemical per-

Corresponding authors: Zhi-yuan Wan E-mail: zhiyuanwang@neuq.edu.cn; Yan-guo Liu E-mail: lyg@neuq.edu.cn

formance improvements [17–19]. In addition, high conductivity Cu is also a promising inactive component to alloy with the active metal and has been successfully introduced into Sn for excellent functional characteristics. However, there is still no report of the use of Cu_2Sb in alkalis ion batteries.

Based on the analysis presented above, herein we put forward a new-type of Cu_2Sb nanoalloy confined in a 3D porous carbon (Cu_2Sb@3DPC) composite anode material fabricated with controllable vacuum freeze-drying followed by a carbon-thermal reduction method. The simultaneous formation of the nanoalloy and the carbon matrix can guarantee good dispersion of active alloys in carbon and avoid the aggregation of a nanoalloy; furthermore, the process can reinforce the binding force between the carbon layer and alloy. The carbon substrate with a 3D porous structure, large active surface area, and excellent conductivity can provide adequate Na^+/K^+ storage sites and a fast ion diffusion/electron transfer path and also offer sufficient interspace to accommodate the volume expansion of Sb during cycling, which can efficiently enhance the structural stability and integrality of the electrode. Cu_2Sb@3DPC is expected to show excellent electrochemical performance in SIBs and PIBs. This versatile strategy can also be used to fabricate other composite electrode materials.

2. Experimental

2.1. Material synthesis

2.5 g citric acid, 0.261 g $Cu(NO_3)_2{\cdot}3H_2O$, 0.2035 g $SbCl_3$, and 20.65 g NaCl were dissolved in deionized water and stirred for 12 h. All of the reagents were analytically pure and used without further disposal. The above solution was frozen for 24 h until completely solidified, and the sample was then transferred into the freeze dryer and dried for 24 h to produce a white powder. The obtained powder was sintered at 600°C for 2 h in mixed H_2/Ar. To remove the NaCl template, the calcined sample was placed in water and then filtered with an aspirator filter pump several times. The sample was transferred to a 110°C oven to evaporate the water. The final sample was named Cu_2Sb@3DPC.

2.2. Material characterization

X-ray diffraction (XRD; Rigaku SmartLab, Cu K_α radiation, 45 kV, 200 mA) was performed to identify the crystal structure of the material. Raman scattering spectra investigated the carbon by an InVia microscope with 532 nm laser (Renishaw). The powder morphology was observed using a scanning electron microscope (SEM, ZEISS SUPRA55, 15 kV). The microstructure was further measured by transmission electron microscopy (HRTEM, JEM 2100F), and the element composition and content were tested by energy-dispersive X-ray spectroscopy. The specific surface area was tested using a surface area analyzer (SSA-4000). X-ray photoelectron spectroscopy (XPS, ESCSLAB 250XI) was adopted to investigate the valence state and elementary composition of the sample.

2.3. Electrochemical measurements

The electrodes were synthesized with Cu_2Sb@3DPC (80wt%), carbon black (10wt%), and polyvinylidene fluoride (PVDF) (10wt%) dissolved in N-methyl-2-pyrrolidinone (NMP). After stirring for 4 h, the obtained slurry was coated on the Cu foil (the loading mass is around 1.5 $mg{\cdot}cm^{-2}$), the anode piece was coated in an air circulation oven at 60°C for 8 h before drying at 120°C under vacuum. To evaluate the potassium-ion storage performance of Cu_2Sb@3DPC, CR2032 type coin cells were adopted and assembled in a glove box (Ar-filled). K metal was used as the counter and reference electrode, glass fiber (Whatman GF/D) was adopted as the separator, 0.8 M KPF_6 in ethylene carbonate and diethyl carbonate (EC : DEC = 1:1 by volume) served as the electrolyte. For SIBs, Na metal was used as the counter and reference electrodes, and the electrolyte was 1 M $NaClO_4$ in a mixture solvent of EC and DEC (volume ratio is 1:1) with 5wt% fluoroethylene carbonate. An electrochemical workstation (CHI 660E) and LANDCT2001A battery test system were employed to evaluate the electrochemical performance of Cu_2Sb@3DPC.

3. Results and discussion

3.1. Structure characterization of the Cu_2Sb@3DPC

The forming process of Cu_2Sb@3DPC is shown in Fig. 1(a). A homogeneous solution containing citric acid, $Cu(NO_3)_2{\cdot}3H_2O$, $SbCl_3$, and NaCl was first obtained. The self-assembly of NaCl cubic precursor covered with the Cu^{2+}/Sb^{2+} complex compound was then formed during the freeze-drying process. During the subsequent carbonization, Cu_2Sb nanoparticles were generated on the surface of the NaCl template *in-situ*, and citric acid was pyrolyzed into carbon at the same time. After the removal of the NaCl template, a Cu–Sb nanoalloy composite anchored on the porous carbon was obtained. As shown in the SEM images of Cu_2Sb@3DPC (Figs. 1(b)–1(c)), an interconnected 3D porous structure, inherited from the NaCl template, was embedded with a number of ultrafine nanoparticles. The TEM results further confirm this morphological feature (Fig. 1(d)) and the average alloy size was estimated as 6.5 nm according to the particle size distribution analysis (Fig. 1(e)). HRTEM was performed to identify the structure of the as-prepared sample. As shown in Fig. 1(f), the observed lattice spacing of 0.29 nm corresponds well to the (110) plane of Cu_2Sb crystal (PDF#65-2851) [20]. A distinct amorphous carbon coating layer, which provides the anchorage site for the Cu_2Sb and restrains the nanoalloy from overgrowth and agglomeration, was observed around the alloy particle. Figs. 1(g)–1(j) show

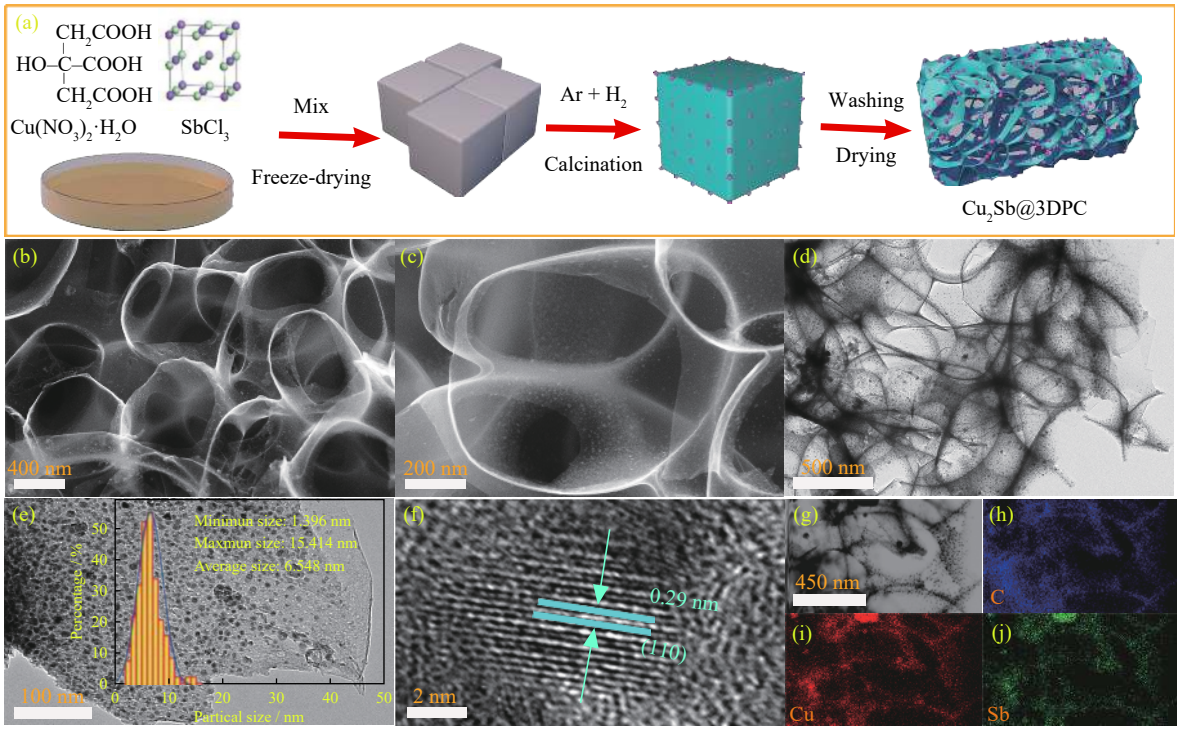

Fig. 1. (a) Schematic diagram of the building-up process, (b, c) SEM images, (d, e) TEM images and particle size distribution (inset of (e)), (f) HRTEM image, and (g–h) the element maps of Cu_2Sb@3DPC.

the element distribution of Cu_2Sb@3DPC; Cu, Sb, and C share the same distribution area, which indicates the interfacial anchoring effect between Cu_2Sb nanoparticles and porous carbon. This porous carbon network is highly conducive to increasing the electronic conductivity of the electrode and releasing the stress of Sb.

The XRD pattern in Fig. 2(a) shows clear and sharp diffraction peaks, which match the standard pattern of Cu_2Sb (PDF#65-2851) and indicates a well crystallinity. There are no obvious diffraction peaks corresponding to carbon, except for a broad peak near 26°, which indicates an amorphous structure. The carbon was further surveyed by Raman spectroscopy. As shown in Fig. 2(b), the obvious Raman peaks at 1342, 1601, and 2920 cm^{-1} are consistent with typical D-band, G-band, and 2D band spectra, respectively [21–22]. The intensity ratio of D-band to G-band (I_D/I_G) was

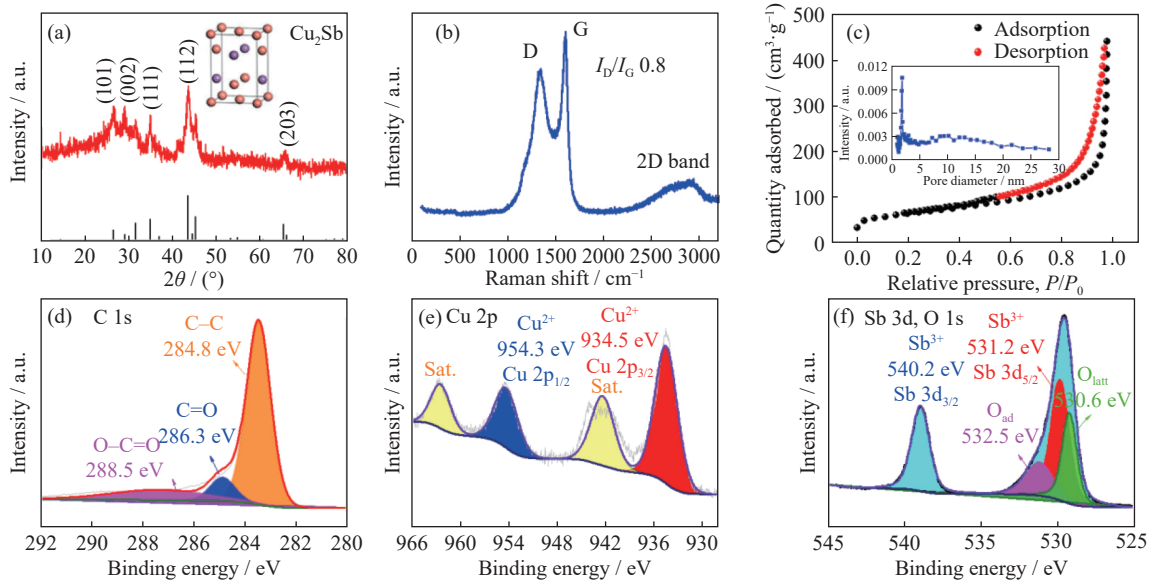

Fig. 2. Structure and composition analysis of Cu_2Sb@3DPC: (a) XRD pattern; (b) Raman spectrum; (c) N_2 adsorption–desorption isotherms and BJH pore size distribution curves (inset). High-resolution XPS spectra: (d) C 1s, (e) Cu 2p, (f) Sb 3d and O 1s.

0.8, indicating a highly disordered degree of carbon, which agrees well with the XRD and TEM results. The disordered carbon structure provides more active storage sites and accommodates the volume expansion of Sb. The nitrogen adsorption–desorption isotherm of Cu_2Sb@3DPC (Fig. 2(c)) presents a type-IV isotherm with an H3-type hysteresis loop, which indicates a mesoporous characteristic. The specific surface area calculated by Brunauer–Emmett–Teller was 173 $m^2 \cdot g^{-1}$ and the pore size was concentrated in the range of 2–20 nm. The affluent porous structure with large available active surface area accelerates the electron transport, facilitates the diffusion of electrolyte ions, and provides abundant space to accommodate the volume expansion of Sb. The 3D porous carbon provides mechanical and conductive support to accommodate the volume changes of Sb, resist the aggregation of the nanoalloy, accelerate the electron transport, and contribute to the capacity based on the pseudocapacitance mechanism. The XPS spectrum was used to confirm the composition and elemental chemical states of Cu_2Sb@3DPC. As shown in Fig. 2(d), the C 1s spectrum can be deconvoluted into three peaks at 284.8, 286.3, and 288.5 eV, which originate from C–C, C=O, and O–C=O [23]. The Cu 2p spectrum shows two signals of 934.5 eV and 954.3 eV with theirs satellite peaks (Sat.) (Fig. 2(e)), which correspond to $2p_{3/2}$ and $2p_{1/2}$ of Cu^{2+} [24]. The peaks at 531.2 eV and 540.2 eV in the Sb 3d spectrum (Fig. 2(f)) represent $3d_{5/2}$ and $3d_{3/2}$ of Sb^{3+}, respectively [25–26]. The O 1s peaks at 530.6 eV and 532.5 eV indicate the lattice oxygen (O_{latt}) and surface-adsorbed oxygen species (O_{ad}), respectively [17]. Oxygen strengthens the interaction between the Cu–Sb alloy and the carbon, which is beneficial to enhancing the structural stability and integrity.

3.2. Electrochemical performance studies of Cu_2Sb@3DPC for SIBs and PIBs

The sodium-ion storage performance of Cu_2Sb@3DPC was first investigated through cyclic voltammetry (CV), which was measured in a potential window from 0.01 to 3.0 V at a scan rate of 0.1 $mV \cdot s^{-1}$. As shown in Fig. 3(a), during the first cycle, there are two main cathodic peaks at 1.02 and 0.01 V. The large, broad cathodic peak at 1.02 V is related to the formation of solid electrolyte interphase (SEI) film on the

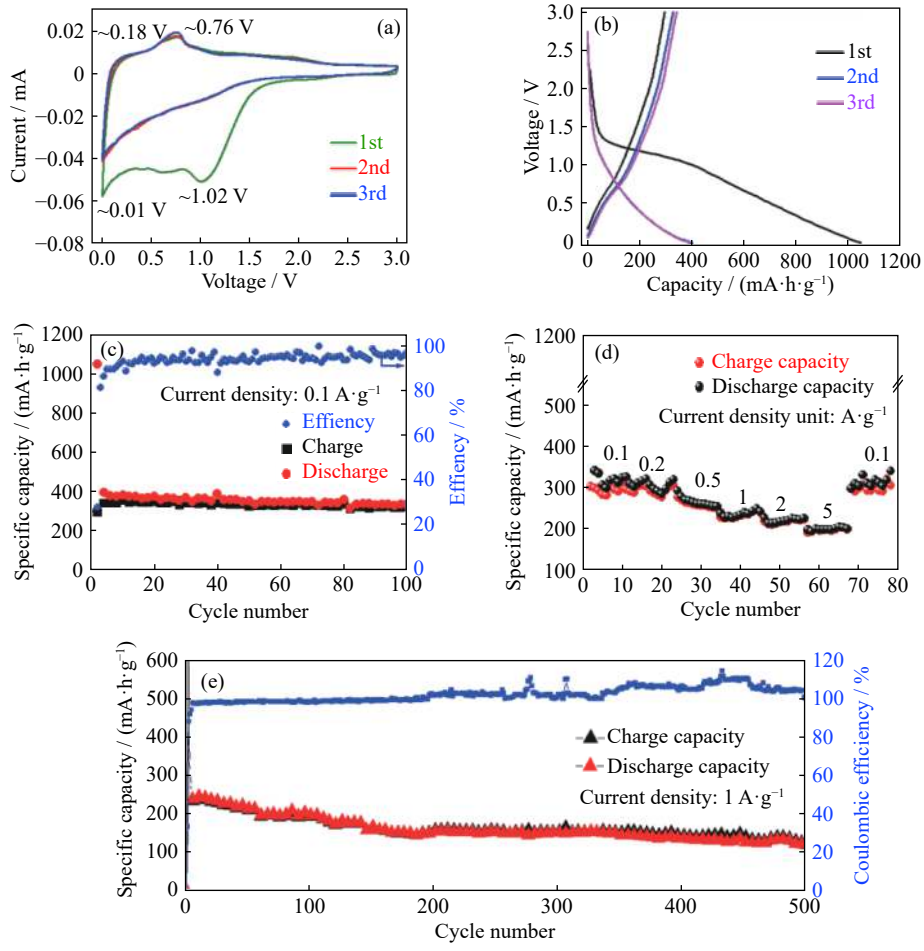

Fig. 3. Electrochemical performance of Cu_2Sb@3DPC in SIBs: (a) CV curves; (b) charge–discharge curves; (c) cycling; (d) rate performance; (e) long cycle performance at 1 $A \cdot g^{-1}$.

electrode surface from the irreversible decomposition of electrolytes and the irreversible intercalation of sodium ions into micropores and defects; this peak disappeared from the second cycle. The cathodic peak around 0.01 V corresponds to the multistep sodiation reaction of Sb to form Na_3Sb and the insertion of Na^+ into carbon. The broad anodic peaks at 0.18 and 0.76 V are attributed to the extraction of Na from the carbon anode and the desodiation reaction of Na_3Sb to NaSb and Sb [27]. From the second cycle, the CV curves overlapped, which reveals remarkable structure stability. Fig. 3(b) displays the first three discharge/charge profiles of Cu_2Sb@3DPC at 0.1 $A\cdot g^{-1}$. Cu_2Sb@3DPC delivers a discharge capacity of 1050.3 $mA\cdot h\cdot g^{-1}$ and a charge capacity of 295.3 $mA\cdot h\cdot g^{-1}$ with a coulomb efficiency (CE) of 28.12% for the first cycle. The low CE is mainly caused by the large specific surface area, the abundant pore structure, and small nanoalloy particle, which leads to a large SEI film and irreversible intercalation [28–29]. After full activation in the first several cycles, the capacity and CE tended to increase and a specific capacity of 328.3 $mA\cdot h\cdot g^{-1}$ with a retention rate of 96.1% (vs. 3rd cycle), and CE of 97% were acquired after 100 cycles, as shown in Fig. 3(c). Furthermore, long-life cycling performance was also investigated, as shown in Fig. 3(e), maintaining a capacity of 131.8 $mA\cdot h\cdot g^{-1}$ with capacity retention of 54.4% after 500 cycles at 1$A\cdot g^{-1}$, and the CE was stable at 99%. The excellent cycling stability is attributed to the well-designed 3D porous composite structure, which can afford the volume expansion of Sb and maintain the integrity of the electrode.

The rate capability of Cu_2Sb@3DPC was evaluated as shown in Fig. 3(d), and it delivers 296, 293, 260, 235, 220, and 199 $mA\cdot h\cdot g^{-1}$ from 0.1 to 5 $A\cdot g^{-1}$, respectively. A capacity of 292 $mA\cdot h\cdot g^{-1}$ was achieved at 0.1 $A\cdot g^{-1}$ after different rate cycling, demonstrating the endurance of the electrode in a rapid charging/discharging procedure. The superior rate property was related to the short ion diffusion path of ultrafine alloy particles and the excellent electronic conductivity of 3D porous network structure. Additionally, the rate capability and cycling performance of Cu_2Sb@3DPC in this work outperformed most previously reported carbon-based anode materials, as shown in Table 1.

Table 1. Performance comparison of Cu_2Sb@3DPC in this work with other carbon-based anode materials for sodium and potassium-ion batteries

Materials	Rate capacity / ($mA\cdot h\cdot g^{-1}$)	Cycling stability / ($mA\cdot h\cdot g^{-1}$)	Ref.	Battery
SnS/SnSb@C	159 (2 $A\cdot g^{-1}$)	270 (0.2 $A\cdot g^{-1}$, 200 cycles)	[30]	SIBs
Fe_7S_8/N-C	327.8 (3.2 $A\cdot g^{-1}$)	406.7 (0.5 $A\cdot g^{-1}$, 500 cycles)	[31]	SIBs
RNSC-800	236 (10 $A\cdot g^{-1}$)	236 (10 $A\cdot g^{-1}$, 5000 cycles)	[32]	SIBs
SUC-4	178 (8 $A\cdot g^{-1}$)	219 (1 $A\cdot g^{-1}$, 500 cycles)	[33]	SIBs
Sb/Sb_2O_3@NCNFs	224 (5 $A\cdot g^{-1}$)	527.3 (0.1 $A\cdot g^{-1}$, 100 cycles)	[34]	SIBs
Cu_2Sb@3DPC	199 (5 $A\cdot g^{-1}$)	328.3 (0.1 $A\cdot g^{-1}$, 100 cycles)	This work	SIBs
CFM-SNG	204.3 (2 $A\cdot g^{-1}$)	188.8 (1 $A\cdot g^{-1}$, 2000 cycles)	[35]	PIBs
$CoSe_2$@NC	120.8 (1 $A\cdot g^{-1}$)	184.5 (0.5 $A\cdot g^{-1}$, 1000 cycles)	[36]	PIBs
NHPC	102.6 (2 $A\cdot g^{-1}$)	119.9 (1 $A\cdot g^{-1}$, 1000 cycles)	[37]	PIBs
$FeSe_2$@C	61 (1.6 $A\cdot g^{-1}$)	182 (0.1 $A\cdot g^{-1}$, 100 cycle)	[38]	PIBs
HCS-SC	81 (10 C)	200 (1C, 200 cycles)	[39]	PIBs
Cu_2Sb@3DPC	148 (5$A\cdot g^{-1}$)	260 (0.1 $A\cdot g^{-1}$, 100 cycles)	This work	PIBs

The potassium-ion storage performance of Cu_2Sb@3DPC was investigated, as demonstrated in Fig. 4. The CV curves of Cu_2Sb@3DPC (Fig. 4(a)) were tested in the potential window of 0.01–3.0 V at 0.1 $mV\cdot s^{-1}$. The peak intensity was relatively weaker than that in SIBs, which may be related to the larger ion radium and resultant lower ion diffusion coefficient. The reduction peak at ~0.01 V corresponds to the intercalation of K in carbon [40–41], the peak at ~0.2 V is related to the alloying reaction of Sb with K, and the peak at 0.59 V reflects the formation of an SEI layer [42–43], which disappeared in the following cycles. The broad oxidation peaks at 0.33 and 1.5 V indicate the extraction of K from carbon and the formation of the K_xSb phase [44–45].

Fig. 4(b) reveals the charge/discharge curves of Cu_2Sb@3DPC under 0.1 $A\cdot g^{-1}$ from 0.01 to 3.0 V. The initial discharge and charge capacity were 1480.7 and 302.5 $mA\cdot h\cdot g^{-1}$, respectively. After the first circulation, the curves were coincident, which shows perfect cycle reversibility of the electrode. Figs. 4(c) and 4(e) show the cyclic performance of Cu_2Sb@3DPC. After the activation reaction for the first several cycles, the reversible capacity remained stable, and the electrode delivered a capacity retention of 86% after 100 cycles at 0.1 $A\cdot g^{-1}$ with a specific capacity of 260 $mA\cdot h\cdot g^{-1}$ and of 68.2% after 500 cycles at 1 $A\cdot g^{-1}$. The rate property of Cu_2Sb@3DPC is shown in Fig. 4(d). Cu_2Sb@3DPC delivered 285, 236, 203, 187, 170, and 148 $mA\cdot h\cdot g^{-1}$ from 0.1 to 5 $A\cdot g^{-1}$. A high specific capacity of 233 $mA\cdot h\ g^{-1}$ at 0.1 $A\cdot g^{-1}$ can be obtained after charging and discharging under a

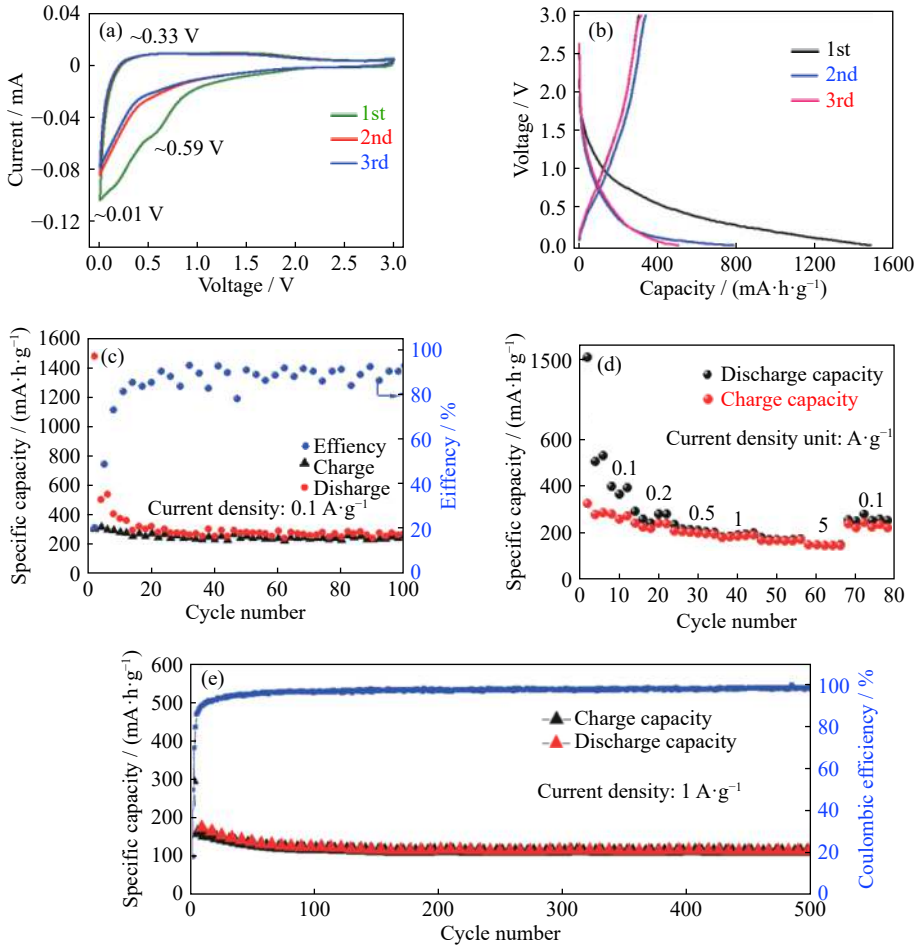

Fig. 4. (a) CV curves, (b) charge-discharge curves, (c) cycle performance, (d) rate performance, and (e) long cycle performance at 1 $A \cdot g^{-1}$ of Cu_2Sb@3DPC in PIBs.

high current. Furthermore, SEM was conducted after 100 cycles in both SIBs and PIBs to verify the structural stability of Cu_2Sb@3DPC. As shown in Figs. 5(a)–5(d), the Cu_2Sb@3DPC structure remained intact without obvious damage after 100 cycles at a current density of 0.1 $A \cdot g^{-1}$ in SIBs and PIBs, confirming the stability of the 3D porous structure.

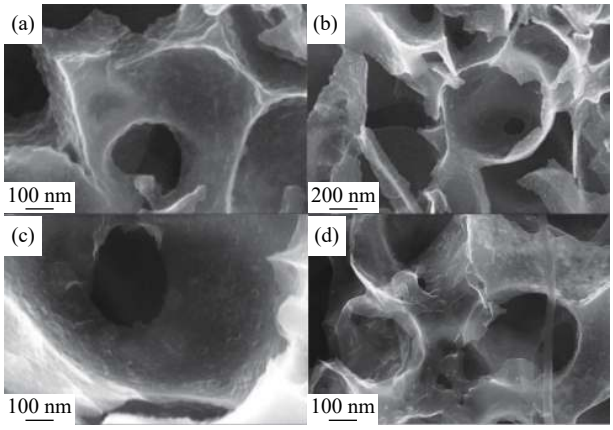

Fig. 5. SEM images of the Cu_2Sb@3DPC electrode after 100 cycles at 0.1 $A \cdot g^{-1}$ in (a, b) SIBs and (c, d) PIBs.

The CV tests under different scanning speeds (0.2, 0.6, 1.0, 2.0, 4.0 $mV \cdot s^{-1}$) were performed to understand the electrochemical energy storage mechanism of Cu_2Sb@3DPC (Fig. 6). With the increasing scanning rate, the CV curves displayed a similar tendency, except for the increase in peak intensity and the slight change in the peak position, demonstrating similar electrochemical behavior. The electrochemical process can be characterized by the following equations [46–47].

$$i = av^b \tag{1}$$

$$\lg i = \lg a + b \lg v \tag{2}$$

where i represents the current, v represents scanning speed, and a/b are constants. If b approaches 0.5, it is a diffusion-controlled kinetic process; if b approaches 1, it is a capacitance-contributed dynamic process; if the b value is between 0.5 and 1, the reaction process is co-controlled by both mechanisms. The value of b can be calculated from the linear relation of lg i and lg v, and it was 0.9 for SIBs and 0.86 for PIBs, indicating that the surface-induced capacitive process is the dominant mechanism. To quantitatively analyze the percent-

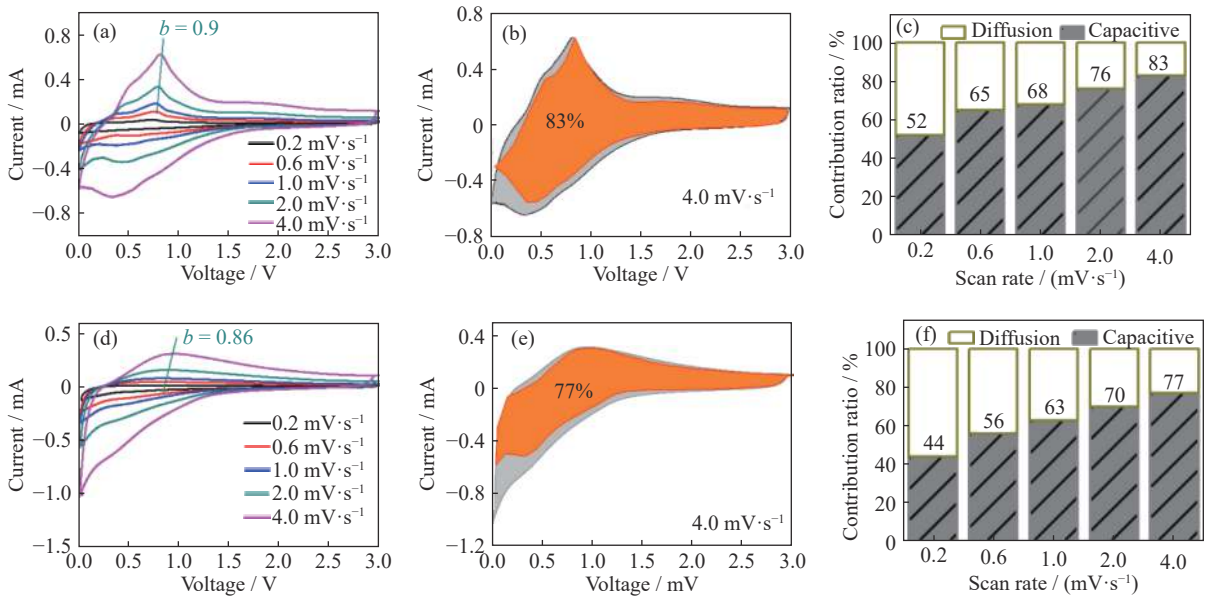

Fig. 6. CV curves of Cu_2Sb@3DPC (a, d), capacitive contribution (orange) and diffusion contribution (gray) at 4.0 mV·s^{-1} (b, e), and the ratio of the capacitive contribution and diffusion-controlled portion under different scan rates (c, f) in SIBs and PIBs, respectively.

age of capacitor contribution, the following equation can be mentioned [48–49]:

$$i(v) = k_1 v + k_2 v^{1/2} \quad (3)$$

where k_1 and k_2 mean constants at a particular voltage.

In the above equation, $k_1 v$ represents the capacitive effect part, $k_2 v^{1/2}$ reflects the diffusion-controlled redox reaction process, and k_1 and k_2 can be calculated from the i values under the same voltage. With scan rate increase (0.2, 0.6, 1.0, 2.0, 4.0 mV·s^{-1}), the surface-induced capacitive contributions gradually increase for both SIBs and PIBs. As the scan rates increase from 0.2 to 4.0 mV·s^{-1}, the pseudocapacitance-controlled contribution ratios gradually increase from 52% to 83% for SIBs and from 44% to 77% for PIBs. This result means that the diffusion contribution is dominant at low scan rates, while the capacitive storage reaction delivers greater contribution at high scan rates (Figs. 6(b) and 6(e)), which can reasonably explain the good rate performance [50–51]. The high capacitive contribution is related to the disordered porous carbon structure, which provides sufficient active sites for the fast insertion and removal of K^+/Na^+.

4. Conclusion

Simple and feasible freeze-drying followed by a thermal reduction method was employed to prepare Cu_2Sb@3DPC composite. Benefiting from the rational structure design with ultrafine alloy particles and an interconnected 3D porous structure, the electrode exhibits a high capacity, excellent cycling performance, and rate property in both SIBs and PIBs. The porous carbon architecture effectively restrains the volume expansion of Sb and nano Cu_2Sb aggregation. The ultrafine alloy shortens the diffusion path of K^+/Na^+; the large specific surface area with the disordered carbon structure promotes ion storage and guarantees sufficient electrical contact between active materials and electrolytes. The strengthened interaction between the Cu–Sb alloy and the carbon guarantees excellent structure stability. In addition, the capacitive control process verified by CV explains the excellent rate capacity. This strategy has profound guiding significance for the design and synthesis of alloy anode materials.

Acknowledgements

This study was financially supported by the National Natural Science Foundation of China (Nos. 51871046, 51902046, 52071073, 51874079, 51571054, 51771046, and 51674068), the Natural Science Foundation of Liaoning Province, China (No. 201602257), Natural Science Foundation of Hebei Province, China (Nos. E2019501097, E2018501091, E2020501004), the Science and Technology Project of Hebei Province, China (No. 15271302D), and the Fundamental Research Funds for the Central Universities, China (Nos. N182304017, N182304015, N172302001, N172304044).

References

[1] J.M. Chen, Y. Cheng, Q.B. Zhang, C. Luo, H.Y. Li, Y. Wu, H.H. Zhang, X. Wang, H.D. Liu, X. He, J.J. Han, D.L. Peng, M.L. Liu, and M.S. Wang, Designing and understanding the superior potassium storage performance of nitrogen/phosphorus co-doped hollow porous bowl-like carbon anodes, *Adv. Funct. Mater.*, 31(2021), No. 1, art. No. 2007158.

[2] B. Chen, D.L. Chao, E.Z. Liu, M. Jaroniec, N.Q. Zhao, and S.Z. Qiao, Transition metal dichalcogenides for alkali metal ion batteries: Engineering strategies at the atomic level, *Energy Environ. Sci.*, 13(2020), No. 4, p. 1096.

[3] J.C. Pramudita, D. Sehrawat, D. Goonetilleke, and N. Sharma, An initial review of the status of electrode materials for potassium-ion batteries, *Adv. Energy Mater.*, 7(2017), No. 24, art. No. 1602911.

[4] X.D. He, Z.H. Liu, J.Y. Liao, X. Ding, Q. Hu, L.N. Xiao, S. Wang, and C.H. Chen, A three-dimensional macroporous antimony@carbon composite as a high-performance anode material for potassium-ion batteries, *J. Mater. Chem. A*, 7(2019), No. 16, p. 9629.

[5] J. Zheng, Y. Yang, X.L. Fan, G.B. Ji, X. Ji, H.Y. Wang, S. Hou, M.R. Zachariah, and C.S. Wang, Extremely stable antimony–carbon composite anodes for potassium-ion batteries, *Energy Environ. Sci.*, 12(2019), No. 2, p. 615.

[6] Y.L. An, Y. Tian, L.J. Ci, S.L. Xiong, J.K. Feng, and Y.T. Qian, Micron-sized nanoporous antimony with tunable porosity for high-performance potassium-ion batteries, *ACS Nano*, 12(2018), No. 12, p. 12932.

[7] G.H. Wang, X.H. Xiong, Z.H. Lin, C.H. Yang, Z. Lin, and M.L. Liu, Sb/C composite as a high-performance anode for sodium ion batteries, *Electrochim. Acta*, 242(2017), p. 159.

[8] J. Qin, T.S. Wang, D.Y. Liu, E.Z. Liu, N.Q. Zhao, C.S. Shi, F. He, L.Y. Ma, and C.N. He, A top-down strategy toward SnSb in-plane nanoconfined 3D N-doped porous graphene composite microspheres for high performance Na-ion battery anode, *Adv. Mater.*, 30(2018), No. 9, art. No. 1704670.

[9] P.X. Xiong, J.X. Wu, M.F. Zhou, and Y.H. Xu, Bismuth-antimony alloy nanoparticle@porous carbon nanosheet composite anode for high-performance potassium-ion batteries, *ACS Nano*, 14(2020), No. 1, p. 1018.

[10] J. Han, K.J. Zhu, P. Liu, Y.C. Si, Y.J. Chai, and L.F. Jiao, N-doped CoSb@C nanofibers as a self-supporting anode for high-performance K-ion and Na-ion batteries, *J. Mater. Chem. A*, 7(2019), No. 44, p. 25268.

[11] Y.P. Li, Q.B. Zhang, Y.F. Yuan, H.D. Liu, C.H. Yang, Z. Lin, and J. Lu, Surface amorphization of vanadium dioxide (B) for K-ion battery, *Adv. Energy Mater.*, 10(2020), No. 23, art. No. 2000717.

[12] X.F. Ge, S.H. Liu, M. Qiao, Y.C. Du, Y.F. Li, J.C. Bao, and X.S. Zhou, Enabling superior electrochemical properties for highly efficient potassium storage by impregnating ultrafine Sb nanocrystals within nanochannel-containing carbon nanofibers, *Angew. Chem. Int. Ed.*, 58(2019), No. 41, p. 14578.

[13] M.C. Schulze, R.M. Belson, L.A. Kraynak, and A.L. Prieto, Electrodeposition of Sb/CNT composite films as anodes for Li- and Na-ion batteries, *Energy Storage Mater.*, 25(2020), p. 572.

[14] X.W. Liu, M. Gao, H. Yang, X.W. Zhong, and Y. Yu, 2D sandwich-like nanosheets of ultrafine Sb nanoparticles anchored to graphene for high-efficiency sodium storage, *Nano Res.*, 10(2017), No. 12, p. 4360.

[15] C. Nita, J. Fullenwarth, L. Monconduit, L. Vidal, and C. Matei Ghimbeu, Influence of carbon characteristics on Sb/carbon nanocomposites formation and performances in Na-ion batteries, *Mater. Today Energy*, 13(2019), p. 221.

[16] Q.Q. Yang, J. Zhou, G.Q. Zhang, C. Guo, M. Li, Y.C. Zhu, and Y.T. Qian, Sb nanoparticles uniformly dispersed in 1-D N-doped porous carbon as anodes for Li-ion and Na-ion batteries, *J. Mater. Chem. A*, 5(2017), No. 24, p. 12144.

[17] Z.Y. Wang, K.Z. Dong, D. Wang, S.H. Luo, X. Liu, Y.G. Liu, Q. Wang, Y.H. Zhang, A.M. Hao, C.N. He, C.S. Shi, and N.Q. Zhao, Constructing N-Doped porous carbon confined FeSb alloy nanocomposite with Fe–N–C coordination as a universal anode for advanced Na/K-ion batteries, *Chem. Eng. J.*, 384(2020), art. No. 123327.

[18] Z.Y. Wang, K.Z. Dong, D. Wang, S.H. Luo, Y.G. Liu, Q. Wang, Y.H. Zhang, A.M. Hao, C.S. Shi, and N.Q. Zhao, A nanosized SnSb alloy confined in N-doped 3D porous carbon coupled with ether-based electrolytes toward high-performance potassium-ion batteries, *J. Mater. Chem. A*, 7(2019), No. 23, p. 14309.

[19] Z.Y. Wang, C.Q. Duan, D. Wang, K.Z. Dong, S.H. Luo, Y.G. Liu, Q. Wang, Y.H. Zhang, and A.M. Hao, BiSb@Bi_2O_3/SbO_x encapsulated in porous carbon as anode materials for sodium/potassium-ion batteries with a high pseudocapacitive contribution, *J. Colloid Interface Sci.*, 580(2020), p. 429.

[20] L. Baggetto, E. Allcorn, A. Manthiram, and G.M. Veith, Cu_2Sb thin films as anode for Na-ion batteries, *Electrochem. Commun.*, 27(2013), p. 168.

[21] Y.R. Lv, Y.H. Li, C. Han, J.F. Chen, Z.X. He, J. Zhu, L. Dai, W. Meng, and L. Wang, Application of porous biomass carbon materials in vanadium redox flow battery, *J. Colloid Interface Sci.*, 566(2020), p. 434.

[22] H.L. Wang, W.H. Yu, N. Mao, J. Shi, and W. Liu, Effect of surface modification on high-surface-area carbon nanosheets anode in sodium ion battery, *Microporous Mesoporous Mater.*, 227(2016), p. 1.

[23] S.C. Luo, T.Y. Wang, H.Y. Lu, X.Q. Xu, G. Xue, N. Xu, Y. Wang, and D.S. Zhou, Ultrasmall SnO_2 nanocrystals embedded in porous carbon as potassium ion battery anodes with long-term cycling performance, *New J. Chem.*, 44(2020), No. 27, p. 11678.

[24] L.B. Wang, C.C. Wang, N. Zhang, F.J. Li, F.Y. Cheng, and J. Chen, High anode performance of in situ formed Cu_2Sb nanoparticles integrated on Cu foil via replacement reaction for sodium-ion batteries, *ACS Energy Lett.*, 2(2017), No. 1, p. 256.

[25] J.J. Ye, G. Xia, Z.Q. Zheng, and C. Hu, Facile controlled synthesis of coral-like nanostructured Sb_2O_3@Sb anode materials for high performance sodium-ion batteries, *Int. J. Hydrogen Energy*, 45(2020), No. 16, p. 9969.

[26] R. Izquierdo, E. Sacher, and A. Yelon, X-ray photoelectron spectra of antimony oxides, *Appl. Surf. Sci.*, 40(1989), No. 1-2, p. 175.

[27] L. Wu, X.H. Hu, J.F. Qian, F. Pei, F.Y. Wu, R.J. Mao, X.P. Ai, H.X. Yang, and Y.L. Cao, Sb–C nanofibers with long cycle life as an anode material for high-performance sodium-ion batteries, *Energy Environ. Sci.*, 7(2014), No. 1, p. 323.

[28] X.L. Fan, T. Gao, C. Luo, F. Wang, J.K. Hu, and C.S. Wang, Superior reversible tin phosphide-carbon spheres for sodium ion battery anode, *Nano Energy*, 38(2017), p. 350.

[29] Z.M. Liu, X.Y. Yu, X.W. Lou, and U. Paik, Sb@C coaxial nanotubes as a superior long-life and high-rate anode for sodium ion batteries, *Energy Environ. Sci.*, 9(2016), No. 7, p. 2314.

[30] J. Zhu, C.Q. Shang, Z.Y. Wang, J.J. Zhang, Y. Liu, S. Gu, L.J. Zhou, H. Cheng, Y.Y. Gu, and Z.G. Lu, SnS/SnSb@C nanofibers with enhanced cycling stability via vulcanization as an anode for sodium-ion batteries, *ChemElectroChem*, 5(2018), No. 7, p. 1098.

[31] A.H. Jin, M.J. Kim, K.S. Lee, S.H. Yu, and Y.E. Sung, Spindle-like Fe_7S_8/N-doped carbon nanohybrids for high-performance sodium ion battery anodes, *Nano Res.*, 12(2019), No. 3, p. 695.

[32] W.P. Song, J.L. Kan, H.L. Wang, X.C. Zhao, Y.L. Zheng, H. Zhang, L. Tao, M.H. Huang, W. Liu, and J. Shi, Nitrogen and sulfur co-doped mesoporous carbon for sodium ion batteries,

ACS Appl. Nano Mater., 2(2019), No. 9, p. 5643.
[33] Y. Liu and Z.Q. Gao, Synthesis of hierarchically porous nitrogen-doped carbon for sodium-ion batteries, *ChemElectroChem*, 4(2017), No. 5, p. 1059.
[34] D.D. Li, J.Z. Li, J.M. Cao, X.Y. Fu, L. Zhou, and W. Han, Highly flexible free-standing Sb/Sb_2O_3@N-doped carbon nanofiber membranes for sodium ion batteries with excellent stability, *Sustainable Energy Fuels*, 4(2020), No. 11, p. 5732.
[35] W.X. Yang, J.H. Zhou, S. Wang, Z.C. Wang, F. Lv, W.S. Zhang, W.Y. Zhang, Q. Sun, and S.J. Guo, A three-dimensional carbon framework constructed by N/S co-doped graphene nanosheets with expanded interlayer spacing facilitates potassium ion storage, *ACS Energy Lett.*, 5(2020), No. 5, p. 1653.
[36] J. Hu, B. Wang, Q.Y. Yu, D. Zhang, Y.H. Zhang, Y. Li, and W.A. Wang, $CoSe_2$/N-doped carbon porous nanoframe as an anode material for potassium-ion storage, *Nanotechnology*, 31(2020), No. 39, art. No. 395403.
[37] C.L. Gao, Q. Wang, S.H. Luo, Z.Y. Wang, Y.H. Zhang, Y.G. Liu, A.M. Hao, and R. Guo, High performance potassium-ion battery anode based on biomorphic N-doped carbon derived from walnut septum, *J. Power Sources*, 415(2019), p. 165.
[38] T.X. Wang, W.T. Guo, G. Wang, H. Wang, J.T. Bai, and B.B. Wang, Highly dispersed $FeSe_2$ nanoparticles in porous carbon nanofibers as advanced anodes for sodium and potassium ion batteries, *J. Alloys Compd.*, 834(2020), art. No. 155265.
[39] Z.L. Jian, S. Hwang, Z.F. Li, A.S. Hernandez, X.F. Wang, Z.Y. Xing, D. Su, and X.L. Ji, Hard-soft composite carbon as a long-cycling and high-rate anode for potassium-ion batteries, *Adv. Funct. Mater.*, 27(2017), No. 26, art. No. 1700324.
[40] S. Bao, S.H. Luo, S.X. Yan, Z.Y. Wang, Q. Wang, J. Feng, Y.L. Wang, and T.F. Yi, Nano-sized MoO_2 spheres interspersed three-dimensional porous carbon composite as advanced anode for reversible sodium/potassium ion storage, *Electrochim. Acta*, 307(2019), p. 293.
[41] K.S. Huang, Z. Xing, L.C. Wang, X. Wu, W. Zhao, X.J. Qi, H. Wang, and Z.C. Ju, Direct synthesis of 3D hierarchically porous carbon/Sn composites via *in situ* generated NaCl crystals as templates for potassium-ion batteries anode, *J. Mater. Chem. A*, 6(2018), No. 2, p. 434.
[42] C.H. Han, K. Han, X.P. Wang, C.Y. Wang, Q. Li, J.S. Meng, X.M. Xu, Q. He, W. Luo, L.M. Wu, and L.Q. Mai, Three-dimensional carbon network confined antimony nanoparticle anodes for high-capacity K-ion batteries, *Nanoscale*, 10(2018), No. 15, p. 6820.
[43] S.H. Dong, C.X. Li, Z.Q. Li, L.Y. Zhang, and L.W. Yin, Mesoporous hollow Sb/ZnS@C core-shell heterostructures as anodes for high-performance sodium-ion batteries, *Small*, 14(2018), No. 16, art. No. 1704517.
[44] V. Gabaudan, R. Berthelot, L. Stievano, and L. Monconduit, Inside the alloy mechanism of Sb and Bi electrodes for K-ion batteries, *J. Phys. Chem. C*, 122(2018), No. 32, p. 18266.
[45] Y.Y. Yi, W. Zhao, Z.H. Zeng, C.H. Wei, C. Lu, Y.L. Shao, W.Y. Guo, S.X. Dou, and J.Y. Sun, ZIF-8@ZIF-67-derived nitrogen-doped porous carbon confined CoP polyhedron targeting superior potassium-ion storage, *Small*, 16(2020), No. 7, art. No. 1906566.
[46] D.L. Chao, C.R. Zhu, P.H. Yang, X.H. Xia, J.L. Liu, J. Wang, X.F. Fan, S.V. Savilov, J.Y. Lin, H.J. Fan, and Z.X. Shen, Array of nanosheets render ultrafast and high-capacity Na-ion storage by tunable pseudocapacitance, *Nat. Commun.*, 7(2016), art. No. 12122.
[47] W.W. Zhong, J.D. Huang, S.Q. Liang, J. Liu, Y.J. Li, G.M. Cai, Y. Jiang, and J. Liu, New prelithiated V_2O_5 superstructure for lithium-ion batteries with long cycle life and high power, *ACS Energy Lett.*, 5(2020), No. 1, p. 31.
[48] V. Augustyn, P. Simon, and B. Dunn, Pseudocapacitive oxide materials for high-rate electrochemical energy storage, *Energy Environ. Sci.*, 7(2014), No. 5, p. 1597.
[49] T. Brezesinski, J. Wang, S.H. Tolbert, and B. Dunn, Ordered mesoporous α-MoO_3 with iso-oriented nanocrystalline walls for thin-film pseudocapacitors, *Nat. Mater.*, 9(2010), No. 2, p. 146.
[50] Z. Li, C.Z. Zhang, F. Han, F. Wang, F.Q. Zhang, W. Shen, C. Ye, X.K. Li, and J.S. Liu, Towards high-volumetric performance of Na/Li-ion batteries: A better anode material with molybdenum pentachloride–graphite intercalation compounds ($MoCl_5$–GICs), *J. Mater. Chem. A*, 8(2020), No. 5, p. 2430.
[51] C.Z. Zhang, F. Han, J.M. Ma, Z. Li, F.Q. Zhang, S.H. Xu, H.B. Liu, X.K. Li, J.S. Liu, and A.H. Lu, Fabrication of strong internal electric field ZnS/Fe9S10 heterostructures for highly efficient sodium ion storage, *J. Mater. Chem. A*, 7(2019), No. 19, p. 11771.